



Evaluation of sensor types and environmental controls on mapping biomass of coastal marsh emergent vegetation



Kristin B. Byrd ^{a,*}, Jessica L. O'Connell ^b, Stefania Di Tommaso ^b, Maggi Kelly ^b

^a Western Geographic Science Center, United States Geological Survey, 345 Middlefield Road, MS-531, Menlo Park, CA 94025, USA

^b Department of Environmental Science, Policy and Management, University of California, Berkeley, 130 Mulford Hall, #3114, Berkeley, CA 94720-3114, USA

ARTICLE INFO

Article history:

Received 25 October 2013

Received in revised form 29 March 2014

Accepted 2 April 2014

Available online 3 May 2014

Keywords:

Emergent vegetation

Hyperspectral sensor

Field spectroscopy

Multispectral sensor

Water inundation

Blue Carbon

Wetland management

Error reporting

ABSTRACT

There is a need to quantify large-scale plant productivity in coastal marshes to understand marsh resilience to sea level rise, to help define eligibility for carbon offset credits, and to monitor impacts from land use, eutrophication and contamination. Remote monitoring of aboveground biomass of emergent wetland vegetation will help address this need. Differences in sensor spatial resolution, bandwidth, temporal frequency and cost constrain the accuracy of biomass maps produced for management applications. In addition the use of vegetation indices to map biomass may not be effective in wetlands due to confounding effects of water inundation on spectral reflectance. To address these challenges, we used partial least squares regression to select optimal spectral features in situ and with satellite reflectance data to develop predictive models of aboveground biomass for common emergent freshwater marsh species, *Typha* spp. and *Schoenoplectus acutus*, at two restored marshes in the Sacramento–San Joaquin River Delta, California, USA. We used field spectrometer data to test model errors associated with hyperspectral narrowbands and multispectral broadbands, the influence of water inundation on prediction accuracy, and the ability to develop species specific models. We used Hyperion data, Digital Globe World View-2 (WV-2) data, and Landsat 7 data to scale up the best statistical models of biomass. Field spectrometer-based models of the full dataset showed that narrowband reflectance data predicted biomass somewhat, though not significantly better than broadband reflectance data [$R^2 = 0.46$ and percent normalized RMSE (%RMSE) = 16% for narrowband models]. However hyperspectral first derivative reflectance spectra best predicted biomass for plots where water levels were less than 15 cm ($R^2 = 0.69$, %RMSE = 12.6%). In species-specific models, error rates differed by species (*Typha* spp.: %RMSE = 18.5%; *S. acutus*: %RMSE = 24.9%), likely due to the more vertical structure and deeper water habitat of *S. acutus*. The Landsat 7 dataset (7 images) predicted biomass slightly better than the WV-2 dataset (6 images) ($R^2 = 0.56$, %RMSE = 20.9%, compared to $R^2 = 0.45$, RMSE = 21.5%). The Hyperion dataset (one image) was least successful in predicting biomass ($R^2 = 0.27$, %RMSE = 33.5%). Short-wave infrared bands on 30 m-resolution Hyperion and Landsat 7 sensors aided biomass estimation; however managers need to weigh tradeoffs between cost, additional spectral information, and high spatial resolution that will identify variability in small, fragmented marshes common to the Sacramento–San Joaquin River Delta and elsewhere in the Western U.S.

Published by Elsevier Inc.

1. Introduction

Wetlands cover just between 2% and 6% of the earth's land surface, but store a large proportion of the world's carbon in terrestrial soil reservoirs (approximately 15×10^2 petagrams) (Kayranli, Scholz, Mustafa, & Hedmark, 2010). Most of this carbon is found in peatlands, defined as wetland ecosystems with greater than 40 centimeters (cm) of surface organic matter, which represent 16–33% of the global soil carbon pool (Bridgman, Megonigal, Keller, Bliss, & Trettin, 2006).

These significant carbon sinks are primarily a result of on-site (autochthonous) plant production (Moore, 1987). Emergent vegetation of freshwater marshes is particularly productive, with rates of net primary productivity as high as that of tropical forests and intensive agricultural ecosystems (Miller & Fujii, 2010; Rocha & Goulden, 2009). The roots and rhizomes of this vegetation drive soil organic carbon and peat formation (Moore, 1987; Rasse, Rumpel, & Dignac, 2005), resulting in long-term carbon sequestration, soil stability and accretion (Gorham, Lehman, Dyke, Clymo, & Janssens, 2012; Miller, Fram, Fujii, & Wheeler, 2008; Nyman, Walters, Delaune, & Patrick, 2006).

Freshwater marshes, where emergent plant growth leads to peat formation, are found in some of the most significant coastal areas of the United States, including South Florida, the Mississippi River Delta, and the Sacramento–San Joaquin River Delta. The carbon stocks and

* Corresponding author. Tel.: +1 650 329 4279.

E-mail addresses: kbyrd@usgs.gov (K.B. Byrd), jessica.oconnell@okstate.edu (J.L. O'Connell), stefaniaditom@gmail.com (S. Di Tommaso), maggi@berkeley.edu (M. Kelly).

future cumulative carbon storage of these marshes are referred to as "Blue Carbon," and play an important role in managing atmospheric carbon (Pendleton et al., 2012). However freshwater marshes have often been modified by compaction, drainage and oxidation, nutrient enrichment and contamination (Deegan et al., 2012; Deverel & Leighton, 2010; Mishra et al., 2012; Nungesser, 2011; Tornqvist et al., 2008). Marshes are also potentially impacted by sea level rise (National Estuarine Research Reserve System, 2012). If sea level rise is accelerated, coastal marshes characterized by low plant productivity and low sediment supply may experience shifts in the mix of intertidal habitats, leading to loss of vegetation and gains in low marsh and mudflats (Schile et al., 2014; Stralberg et al., 2011; Swanson et al., 2013). The loss or degradation of coastal wetlands could increase net global atmospheric CO₂ inputs by ~6% per year (Hopkinson, Cai, & Hu, 2012). Therefore these ecosystems have been targeted for greenhouse gas (GHG) offset programs, markets and habitat restoration (Emmett-Mattox, Crooks, & Findsen, 2011; McLeod et al., 2011; Pendleton et al., 2012). In particular, soil carbon sequestration in restored peatlands dominated by emergent vegetation may serve an important role in large-scale carbon storage, assuming conditions are optimized to minimize methane emissions (Emmett-Mattox et al., 2011).

There is a need to quantify large-scale plant productivity in coastal marshes to better understand marsh resilience to sea level rise (Schile et al., 2014; Stralberg et al., 2011; Swanson et al., 2013), to help define eligibility for carbon offset credits (Crooks, Emmett-Mattox, & Findsen, 2010), and to monitor contamination (Mishra et al., 2012) and potential eutrophication impacts from surrounding agriculture (Deegan et al., 2012). Aboveground plant biomass is an important input parameter to models that forecast how coastal marsh elevations will respond to sea level rise (Morris & Bowden, 1986; Morris, Sundareshwar, Nietch, Kjerfve, & Cahoon, 2002; Swanson et al., 2013), and it can be used to estimate belowground biomass (Gross, Hardisky, Wolf, & Klemas, 1993) and root:shoot ratios (O'Connell et al. in review). Combining field and remote sensing techniques for estimating biomass of wetland vegetation over large spatial extents will help further these applications. Conventional productivity measurements are labor intensive and destructive to sensitive wetland systems (Zhang, Ustin, Rejmankova, & Sanderson, 1997). Further, while in situ monitoring and field data collection is essential, it is not feasible at the large spatial extents over which change occurs. Given this limitation, satellite observations are required to map vegetation types and provide better estimates of plant production (Goetz & Dubayah, 2011).

Optical remote sensing of the biomass of emergent marsh vegetation has its origins starting in the 1980s, primarily in *Spartina alterniflora*-dominated marshes in the eastern United States, where it was established that biomass can be modeled with vegetation indices such as the normalized difference vegetation index (NDVI) calculated from hand-held radiometer reflectance data (Hardisky, Klemas, & Michael Smart, 1983a; Hardisky, Michael Smart, & Klemas, 1983b; Hardisky, Daiber, Roman, & Klemas, 1984). The use of these indices with Landsat TM images estimated site-wide biomass well in monospecific marshes where vegetation dominated areas several times larger than image pixels (Gross, Hardisky, Klemas, & Wolf, 1987) and in a more species-rich Pacific Coast wetland (Zhang et al., 1997). Given the limitation of moderate resolution images in spatially complex marshes, efforts to map biomass with high resolution images were successful in explaining up to 70% of data variance (Jensen, 1998, 2002). In more current research the application of a red-edge band in an NDVI-type index estimated biomass of wetland vegetation with relatively low error (13% of observed mean biomass) (Mutanga, Adam, & Cho, 2012).

In wetlands along the Pacific Coast of the United States, mapping plant biophysical characteristics poses multiple challenges due to small wetland size, high heterogeneity of vegetation, and varying seasonal and annual patterns of wetland hydrology (Phinn, 1998; Phinn, Stow, & Zedler, 1996). For example in the Sacramento–San Joaquin River Delta, the area of remaining wetlands represents just 3% of its

historical extent (Whipple, Grossinger, Rankin, Stanford, & Askevold, 2012). Optical remote sensing of wetland vegetation is particularly constrained by water inundation and its influence on the relationship between spectral reflectance and field measurements. Field spectra of emergent wetland vegetation show significant reduction in near-infrared reflectance with progressive water depth, which can highly influence NDVI-based estimates for marsh biomass (Beget & Di Bella, 2007; Kearney, Stutzer, Turpie, & Stevenson, 2009). A shift in the red-edge position also occurs with increasing inundation, which could reduce efficacy of red edge position indices in remote sensing applications of inundated vegetation (Turpie, 2013). The vertical stem structure of emergent marsh vegetation canopies poses additional challenges. This structure contributes to high photosynthetic rates by increasing light penetration within canopies. However, vertical stem morphology also increases light scattering and absorption in spaces between vegetation, leading to lower overall canopy reflectance (Mutanga & Skidmore, 2004; Ollinger, 2011).

Vegetation indices generated from hyperspectral or multispectral images can be correlated to plant characteristics through empirical methods, presenting a simple, straightforward and rapid method for detecting biophysical and biochemical plant characteristics while minimizing background effects (Serrano, Peñuelas, & Ustin, 2002; Siciliano, Wasson, Potts, & Olsen, 2008; Thenkabail et al., 2013). However the challenge of NDVI type indices, particularly those based on the red and NIR portion of the spectrum, is that they asymptotically approach a saturation level at high biomass density (Tucker, 1977), and do not estimate biomass well at 100% vegetation cover [a common feature of freshwater marshes (Rocchio, 2005)]. After full canopy cover, unit increases in biomass result in increasingly smaller increases in NIR reflectance, and eventually little or no increase at all, though this may vary with plant biochemistry or canopy structure (Thenkabail, Smith, & De Pauw, 2000). Data saturation problems can be removed with hyperspectral data from several known instruments (e.g., AVIRIS, HypsIRI, EnMap) because of the large number of spectral bands that extend into the shortwave infrared region of the spectrum (Mutanga & Skidmore, 2004; Thenkabail, Enclona, Ashton, & Van Der Meer, 2004b). Narrowband indices calculated from the red-edge region have been used to estimate biomass at full canopy cover in terrestrial grasslands (Mutanga & Skidmore, 2004), however as stated in the above paragraph, indices based on the red-edge region may not be effective in wetland environments because of water inundation effects (Turpie, 2013).

These issues of patch size, data saturation and water inundation need to be considered when developing biomass maps for wetland vegetation. The influence of tidal inundation on the reflectance characteristics of emergent marsh vegetation also needs to be better documented (Klemas, 2013). Hyperspectral and multispectral data have been used to successfully map vegetation at the species level (Belluco et al., 2006; Schmidt & Skidmore, 2003; Wang, Menenti, Stoll, Belluco, & Marani, 2007), and frequencies of tidal inundation can be calculated with LiDAR topographic data (Sadro, Gastil-Buhl, & Melack, 2007). However the use of hyperspectral reflectance data for modeling wetland vegetation biomass has not been evaluated, and a thorough comparison of sensor types for mapping biomass in wetlands based on extensive field data is lacking. Multiple types of imagery are available for biomass mapping at varying cost, spatial and spectral resolution and temporal frequency, and each provides different advantages. A comparison of sensors available for biomass mapping can highlight these tradeoffs, which can then be considered in the context of resources needed for image acquisition and processing.

The primary objective of this study was to compare predictive models of aboveground biomass of common emergent freshwater marsh plant species based on simulated and actual reflectance data from three sensors of varying spectral and spatial resolution. We also explored the influence of environmental controls, particularly water inundation, on model success. To develop predictive models, we used

partial least squares regression (PLS), a multivariate analysis method. We used reflectance data from a field spectrometer to compare simulated narrowband and broadband-based models, to explore the influence of water inundation on biomass estimation, and to test the ability to develop species-specific biomass models. We used satellite data from the hyperspectral, moderate spatial resolution Hyperion sensor, the multispectral, high spatial resolution Digital Globe World View-2 (WV-2) sensor, and the multispectral, moderate spatial resolution Landsat 7 sensor to scale up the best statistical models and produce maps of aboveground biomass over a range of spatial, temporal and spectral resolutions. We identified the best hyperspectral and multispectral bands for biomass prediction, and explored predictive uncertainties of all models, especially for high biomass plots which indicate the production potential of the study marshes.

The main questions addressed in our study include: 1) How well can hyperspectral and multispectral bands derived from field spectrometer data predict aboveground biomass, especially at high biomass values, of two common emergent plant species? 2) How does water inundation influence biomass prediction accuracy and error? 3) Can species-specific biomass models perform better than mixed-species models? 4) What are the associated uncertainties of the predictive statistical models for biomass and biomass maps produced with Hyperion, Landsat 7 and WV-2 satellite imagery?

2. Methods

2.1. Study area

Field measurements were collected at two freshwater wetland sites in the Sacramento–San Joaquin River Delta, San Francisco Bay Estuary, California, USA: Twitchell Island and Sherman Island (Fig. 1). The Twitchell Island site ($38^{\circ} 6' N$, $121^{\circ} 39' W$) is a 6-hectare (ha) experimental impounded freshwater wetland system created in 1997 (Miller & Fujii, 2010; Miller et al., 2008). It is comprised of two ponds permanently flooded to different water depths (25 cm in the west pond and

55 cm in the east pond). This restoration was implemented to study the effect of water depth on peat accretion and carbon storage potential. A network of boardwalks was built within the wetland to reduce disturbance. Twitchell Island is dominated by *Schoenoplectus acutus* (Muhl. ex Bigelow) Á. Löve & D. Löve var. *occidentalis* (S. Watson) S.G. Sm. and a variety of *Typha* species L. and their hybrids (Fig. 2). A dense layer of dead *S. acutus* stems 1 to 2 m tall mixed with other plant litter has accumulated over several years. The ponds are narrow, approximately 75 m wide, and characterized by a high intermixing of emergent marsh species. While the west pond contains virtually no open water areas, the deeper east pond contains three ponds over 1000 m² in size plus additional smaller areas of open water, typically covered by floating aquatic vegetation such as *Lemna* sp. and *Azolla* sp.

The second site was a newly restored wetland, Mayberry Farms, on Sherman Island ($38^{\circ} 03' N$, $121^{\circ} 46' W$). The Mayberry Farms Subsidence Reversal Project was designed to restore approximately 111 ha of impounded freshwater emergent wetlands on land owned by the California Department of Water Resources. The Sherman Island restored wetland was completed fall 2010 and is now dominated primarily by *Typha* spp., with stands of *S. acutus* also present. Interior berms separate four water management units, and allow for access. Due to the young age of the site, litter had mostly not accumulated at the time of sampling. This site was characterized by patches of dense emergent vegetation intermixed with open water. While homogeneous in vegetation composition, patch sized ranged from under 10 m² to over 5000 m². Similar to the Twitchell Island site, the Sherman Island wetland was permanently flooded to maximize peat accretion and carbon sequestration. The elevation at both sites was below sea level, as they are located on islands that experienced significant subsidence resulting from drainage and oxidation (Deverel & Leighton, 2010). Both sites received little sediment from water delivered through intake valves.

Three species of cattails and their hybrids were found in the sites – *T. latifolia* L., *T. angustifolia* L. and *T. domingensis* Pers. These are cosmopolitan species found world-wide and are present in every state in the U.S. *Typha* spp. are normally 1 to 3 m tall and reed-like. *T. latifolia* leaves



Fig. 1. Study area in the Sacramento–San Joaquin River Delta identifying two restored wetlands where sampling occurred during the 2011 and 2012 growing seasons. The Sherman Island site (Mayberry Farms) (right) was restored in 2011 and the Twitchell Island site (left) was restored in 1997. Both sites are continually inundated to maximize peat accretion.

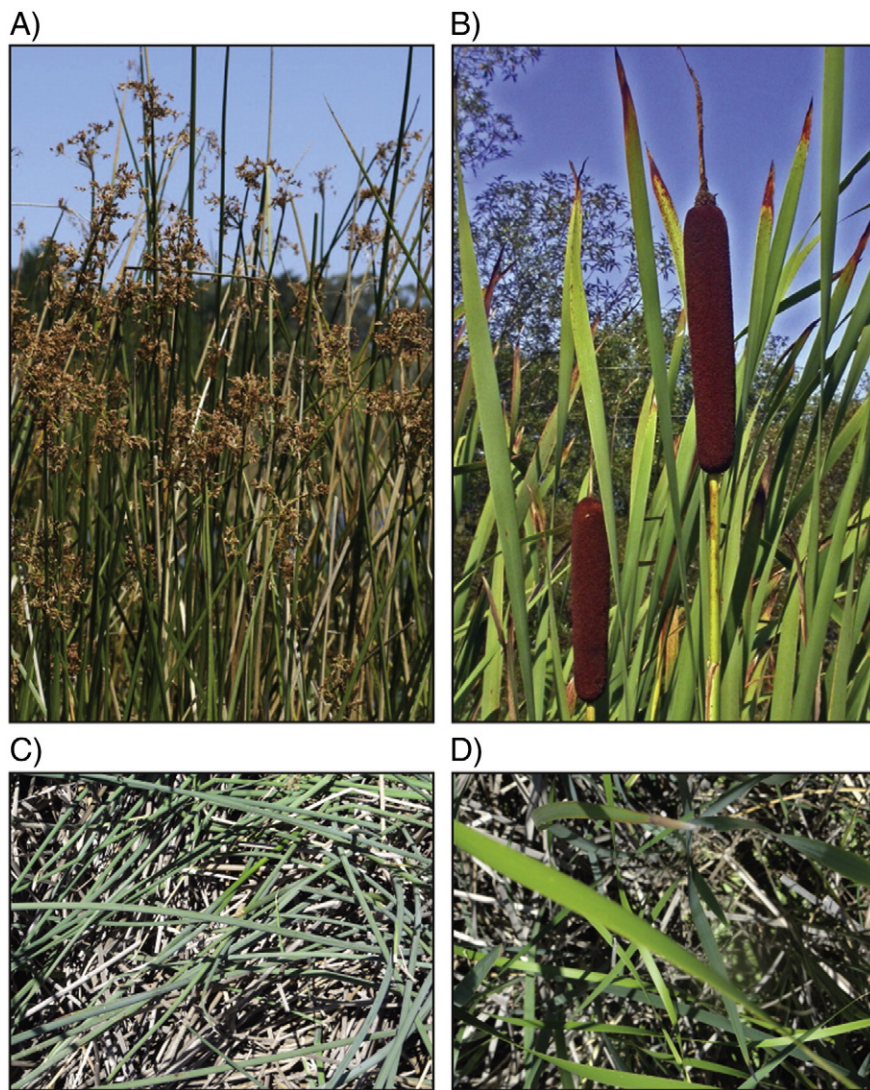


Fig. 2. Photos of A. *Schoenoplectus acutus* (© Eric Hunt), B. *Typha latifolia* (© Neal Kramer), C. above-canopy photo of *S. acutus* displaying substrate of dead standing vegetation, and D. above-canopy photo of *Typha* spp. displaying substrate of dead standing vegetation and floating aquatic vegetation.

are thick, linear, flat, and measure 6 to 29 mm wide, while *T. angustifolia* leaves are 4 to 12 mm wide. *Typha* spp. flower in May and June, and senesce before late October. The spike-like, terminal, cylindrical inflorescence has staminate flowers above and pistillate flowers below. Where *T. angustifolia* and *T. latifolia* occur together, *T. angustifolia* usually colonizes the deeper waters (80 cm or more) (Stevens & Hoag, 2000; USDA Forest Service, 2013b).

S. acutus is characterized by tall rounded green stems 1 to 2 cm thick growing one to four meters tall with an erectophile leaf angle distribution that maximizes exposure to light and photosynthetic rates (Rocha & Goulden, 2009). It is capable of growing in water depths up to 150 cm. *S. acutus* occurs from Nova Scotia and Newfoundland west to southern British Columbia and south to North Carolina, Arkansas, Texas, and California. Leaves are reduced to basal sheaths with blades up to 8 cm long. The inflorescence is a terminal panicle of 3 to 10 spikes which are made up of up to 50 or more spikelets (Tilley, 2012; USDA Forest Service, 2013a).

2.2. Field methods

The east and west ponds on Twitchell Island were sampled during the 2011 growing season, from May through September; Twitchell Island wetlands and Sherman Island wetlands both were sampled

during the 2012 growing season. Sherman Island was not sampled in 2011 because vegetation had not yet established in this newly restored wetland. During each growing season, 40 to 50 permanent plots were designated at each site, spaced 15 m apart along either the berm or boardwalk, to generate an even sampling distribution across the site. Each plot location was recorded with a sub-meter accuracy global positioning system (GPS). GPS points were post-processed to obtain an average spatial accuracy of 0.5 m. Each location was sampled approximately every 3 weeks from mid-May through end of September for a total of 7 sampling dates each year. A total of 540 data points were collected over 2 years, and 226 points had water depths less than 15 cm.

At each sampling date, we recorded the following data within a 1 m² quadrat at each point: absolute percent cover of live emergent vegetation, percent cover of dead vegetation, percent cover of floating aquatic vegetation, average plant height, and water depth (measured three times and averaged). Percent cover variables were estimated visually and assigned one of seven cover categories (0: no cover; 1: 0–1%; 2: 1–5%; 3: 5–25%; 4: 25–50%; 5: 50–75%; 6: 75–95%; 7: 95–100%) (Barbour, Burk, Pitts, Gilliam, & Schwartz, 1999).

Within a 0.1 m² quadrat nested in the 1 m² quadrat, live green biomass of all plants was estimated using allometric equations established by Miller and Fujii (2010). Measurements including plant height,

diameter at 50 cm, number of leaves, and presence of flowers, and were input into species specific allometric equations. The equations were developed at Twitchell Island using approximately 800 *S. acutus* plants and almost 2200 *Typha* spp. plants. The explained variance (R^2) for the *S. acutus* model in Miller and Fujii's (2010) study was 0.92; R^2 for the *T. latifolia* model was 0.9, and R^2 for the *T. angustifolia/T. domingensis* model was 0.92. Neither the time of sample collection nor water depth affected the allometric relationships in Miller and Fujii's study.

2.2.1. Field spectrometer data

Canopy reflectance spectra were obtained over each plot within one day of biomass sampling using an ASD Inc. FieldSpec Pro FR (Analytical Spectral Devices, Inc., Boulder, CO, USA) portable spectroradiometer. Data were collected within two hours before or after solar noon under clear atmospheric conditions. Spectral readings were sampled every 1.4 nm over 350–1000 nm and 2 nm over 1000–2500 nm using a 25° field of view foreoptics. Readings were taken at nadir above the canopy at a consistent height of 4 m from ground level using a 3-m optical fiber cable, producing a field of view of 1.8 m. The 3-m fiber optic cable was attached to a camera monopod that was topped by a camera mounting pan-tilt head with two quarter-inch thumbscrews and a three axis camera bubble level. A pistol grip held the sensor and was attached to the mounting head with one of the thumbscrews. In the first year of data collection, a digital camera was attached with the other thumb screw to take over-canopy at-nadir photos. Before collecting field spectra, the mounting head angle was adjusted so that the pistol grip pointed in the at-nadir position. Upon taking the reflectance measurement, the monopod was raised to a consistent height, and the operator observed the level to ensure that the pistol grip remained in the nadir position.

We calculated canopy reflectance as the ratio of canopy radiance to radiance measured from a calibrated white reference (Spectralon® Labsphere, Inc.). We collected white reference measurements every 10 min. To measure spectral reflectance, ten reflectance measurements, each an average of 12 spectra, were collected and averaged using ViewSpec™ Pro 6.1.10 (Analytical Spectral Devices, Inc., Boulder, CO, USA).

In addition, to aid in production of a vegetation map of the sites, we collected pure spectra of marsh features to serve as endmembers in a multiple endmember spectral mixture analysis (MESMA) (Roberts et al., 1998). MESMA models measure spectra as linear combinations of pure spectra, called endmembers, while allowing the types and number of endmembers to vary on a per pixel basis. This method enables vegetation to be characterized by a unique set of endmembers and their fractions. Features of the marsh other than the emergent vegetation included open water, dead standing vegetation (plant litter), and

floating aquatic vegetation. Five spectra were collected at the canopy level of each feature by positioning the sensor 0.5 m above the ground at nadir to generate a field of view of 0.22 m.

Given the background absorptions and reflectance of the surrounding litter and other vegetation, we tested whether empirical models derived from first order derivative reflectance spectra would perform well in estimating biomass. We generated first order derivative spectra in ViewSpec™ Pro 6.1.10 by calculating the slope of the spectrum every five nm. First derivative spectra are useful for reducing the effects of multiple scattering of radiation resulting from sample geometry and surface roughness (de Jong, 1998). First derivative spectra also enhance absorption features and inflection points masked by interfering background absorptions and canopy background effects (Demetriades-Shah, Steven, & Clark, 1990; Dawson & Curran, 1998; Kochubey & Kazantsev, 2012).

To test both hyperspectral reflectance bands and hyperspectral first order derivative bands for biomass prediction, we simulated 164 Hyperion reflectance bands and 164 Hyperion first order derivative bands with the field spectrometer data in ViewSpec™ Pro 6.1.10. Hyperion has a 30-m spatial resolution and 242 bands each 10 nm-wide. Hyperion reflectance bands were simulated by averaging sets of 10 1-nm ASD field spectrometer reflectance bands centered on each Hyperion band's average wavelength. Simulated Hyperion bands covered the ranges 422–1300 nm, 1443–1795 nm, and 1998–2400 nm. Water absorption regions of the spectrum with high noise were removed from analysis. Hyperion bands were simulated because we acquired imagery from this sensor through a USGS Data Acquisition Request (<https://eo1.usgs.gov/dar/instructions>).

We also simulated WV-2 bands with the field spectrometer data. WV-2 is a commercial satellite sensor with 8 bands and 2 m spatial resolution, an average revisit time of 1.1 days, and includes a coastal blue, blue, green, yellow, red, red edge, and two near infrared bands. Finally, we simulated Landsat 7 Enhanced Thematic Mapper + bands. Landsat 7 is 30 m-resolution with a revisit time of 16 days and contains 6 spectral bands in the 450 to 2350 nm range, including two shortwave infrared bands. The simulation of WV-2 and Landsat 7 bands followed the same approach used for simulation of Hyperion bands.

2.3. Image acquisition

Hyperion scenes were collected for our sites on August 24, 2012 and August 26, 2012 (one scene each per site). Data was downloaded from <http://earthexplorer.usgs.gov/>. We collected Landsat 7 surface reflectance Climate Data Record (CDR) scenes from seven dates from May through September, 2012 (Table 1) (<http://earthexplorer.usgs.gov/>). Image dates were selected to correspond within a week of field biomass

Table 1
Summary statistics of biomass data (g/m^2) coupled with four sets of reflectance data: field spectrometer, Hyperion image, Landsat 7 images, and World View-2 images; n = sample size of datasets for partial least squares regression models.

Data source	Date(s) acquired	n	Mean	Std. Dev.	Min	Max
Field spectrometer	05/2011–09/2011, 05/2012–09/2012	539	987.5	825.4	0.0	5233.8
<i>Typha</i> spp.		247	1138.5	995.5	2.7	5233.8
<i>S. acutus</i>		135	770.6	458.9	31.6	2345.6
water <15 cm		226	1037.3	921.1	0.0	5233.8
Sherman Island		101	1834.1	1090.7	70.8	5233.8
Twitchell Island		438	790.4	599.3	0	4113.7
Hyperion	8/24/2012*, 8/26/2012*	23	1598.6	839.5	528.4	4113.7
Landsat 7	5/23/2012, 6/8/2012, 7/10/2012, 7/26/2012, 8/11/2012, 9/12/2012*, 9/28/2012	64	1312.9	935.8	186.5	5233.8
WV-2	5/12/2011, 6/11/2011, 7/2/2012, 8/8/2012, 9/2/2012*, 9/7/2012*	160	1155.7	932.3	11.3	5233.8

* Image used to create biomass map.

and spectrometer data collection. WV-2 data was obtained free of charge from the Commercial Remote Sensing Space Policy Commercial Imagery Derived Requirements Tool (<https://cidr.cr.usgs.gov/>). We obtained imagery for two dates in spring 2011 and for four dates in summer 2012 (Table 1).

2.4. Image preprocessing

The datum for WV-2 images was converted from WGS 1984 to NAD83 UTM 10 N using the Raster tool with bilinear interpolation in ArcGIS 10.1 (ESRI Corporation, Redlands, CA, USA). Additionally, images were georeferenced using ground control points collected with a Trimble GeoXT hand-held sub-meter GPS with field computer (Trimble Navigation Limited, Sunnyvale, California, USA). Root mean square error (RMSE) of georeferencing for rectified images was less than one half pixel for each image.

We used ENVI 4.7 (EXELIS, McLean, Virginia, USA) to perform radiometric correction of WV-2 and Hyperion imagery to at-sensor radiance ($\text{W m}^{-2} \text{ nm}^{-1} \text{ st}^{-1}$). The Hyperion sensor is a push-broom imaging spectrometer and spectral curvature artifacts are introduced into some bands, particularly the VNIR, limiting the usefulness of these bands without additional correction procedures (Dadon, Ben-Dor, & Karnieli, 2010). We removed uncalibrated bands 1–7, 57–77 and 294–295 from our analysis before conversion to at-sensor radiance. We also removed bands 116–129 in the water absorption region of 1305–1437 nm and bands 165–184 in the water absorption region of 1800–1991 nm. For WV-2 imagery, we used a standard procedure to transform at-sensor radiance into surface reflectance. We used the MODerate resolution TRANsmittance (MODTRAN)-cored Fast Line-of-site Atmospheric Analysis of Spectral Hypercubes (FLAASH) package within ENVI. FLAASH uses a robust procedure to correct for atmospheric attenuation and adjacency effects (ITT Visual Information Solutions, 2009).

For Hyperion satellite imagery, atmospheric correction using the FLAASH algorithm was attempted, but provided poor correction values. Song, Woodcock, Seto, Lenney, and Macomber (2001) suggested that atmospheric correction is most important for multi-image analyses where a common radiometric scale is assumed among images, but might be omitted for analysis of a single image. Following similar protocol to other researchers (Thenkabail, Enclona, Ashton, Legg, & De Dieu, 2004a; Thenkabail et al., 2013), we used at-sensor radiance as our spectral measurement within the single Hyperion image available for each study site.

The Landsat 7 surface reflectance CDR products were generated from the Landsat Ecosystem Disturbance Adaptive Processing System (LEDAPS) (Masek et al., 2013). The LEDAPS software applies Moderate Resolution Imaging Spectroradiometer (MODIS) atmospheric correction routines to Level-1 Landsat Thematic Mapper (TM) or Enhanced Thematic Mapper Plus (ETM+) data. Water vapor, ozone, geopotential height, aerosol optical thickness, and digital elevation are input with Landsat data to the Second Simulation of a Satellite Signal in the Solar Spectrum (6S) radiative transfer models to generate top of atmosphere (TOA) reflectance, surface reflectance, brightness temperature, and masks for clouds, cloud shadows, adjacent clouds, land, and water (Masek et al., 2006).

2.5. Statistical analysis

Partial least squares regression (PLS), a multivariate analysis for selecting optimal spectral features, is increasingly used to develop predictive models of biophysical and biochemical plant parameters (Hansen & Schjoerring, 2003). PLS uses eigenvector-based techniques to reduce many multicollinear predictors, such as spectral data, to independent components that maximize correlation among predictors and a single response variable (Geladi & Kowalski, 1986; Mevik & Cedervist, 2004). Instead of selecting a few spectral bands as predictors as with spectral vegetation indices, PLS extracts the most useful information

from all available measured spectra into non-correlated components (Geladi & Kowalski, 1986) or latent variables (Mevik & Wehrens, 2007). Information on background effects, such as substrate, plant litter and other vegetation cover, are relegated to components that contribute less to the prediction of the key biophysical or biochemical parameter, which reduces model error (Chen, Gu, Shen, Tang, & Matsushita, 2009).

The general underlying model of multivariate PLS is

$$\begin{aligned} X &= TP^T + E \\ Y &= UQ^T + F, \end{aligned}$$

where X is an $n \times m$ matrix of predictors, Y is an $n \times p$ matrix of responses; T and U are $n \times l$ matrices that are, respectively, projections of X (the X score, component or factor matrix) and projections of Y (the Y scores); P and Q are, respectively, $m \times l$ and $p \times l$ orthogonal loading matrices; and matrices E and F are the error terms, assumed to be independent and identically distributed random normal variables (Geladi & Kowalski, 1986).

We examined correlations between live green aboveground biomass and canopy reflectance using PLS with the PLS package in R (Mevik & Wehrens, 2007). We minimized model overfitting by selecting the number of components corresponding to the first local minima for RMSE of prediction, estimated using leave-one-out cross validation (Mevik & Wehrens, 2007). Components include loading values for each band in the dataset; we analyzed these loading values to identify those bands most important for biomass prediction. We built PLS models using a random subset as training data (80% of samples) and compared RMSE of prediction on our validation dataset (the remaining 20% of samples).

Before data analysis we square-root transformed biomass values to produce a normal distribution and minimize the number of outliers. We tested for outliers on the square-root transformed dataset with boxplots and histograms and the modified Thompson tau technique, a statistical method suitable for identifying individual outliers in large sample sizes (Thompson, 1935). The Thompson tau method tests whether the absolute value of the deviation between the highest value and the sample mean is significantly greater than the modified Thompson tau value times the sample standard deviation at the 95% confidence level. One outlier was identified from this analysis.

2.5.1. Field spectrometer-based models

First, we tested regression models with simulated Landsat 7, Hyperion, and WV-2 satellite spectra as predictors, separately for each sensor (Table 2). As a response variable we used square-root transformed

Table 2

Summary of partial least squares regression models generated with field spectrometer reflectance data and image reflectance data.

Field spectrometer reflectance data	Simulated Hyperion bands Pooled dataset Low water subset (<15 cm) Species-specific models (<i>Typha</i> spp. and <i>S. acutus</i>) Simulated Hyperion first order derivative spectrum bands Pooled dataset Low water subset (<15 cm)
Satellite image reflectance data	Simulated Landsat 7 bands Pooled dataset Low water subset (<15 cm) Simulated World View-2 bands Pooled dataset Low water subset (<15 cm)
	Hyperion bands Landsat 7 bands World View-2 bands

Table 3

Distribution of biomass plots sampled in the 2011 and 2012 growing seasons according to water depth and species.

Species	Water depth (cm)								Total
	0–15	16–30	31–45	46–60	61–75	76–90	91–110	Total	
Mixed species	61	32	35	13	6	7	3	157	
<i>Typha</i> spp.	145	55	14	10	4	3	16	247	
<i>S. acutus</i>	20	16	30	32	18	13	6	135	
Total	226	103	79	55	28	23	25	539	

field measured aboveground biomass (g/m^2) for all plots (pooled dataset, $n = 539$; **Table 3**). Next, to test the effect of water inundation on biomass predictions, we subset the field biomass data to plots with water depth less than 15 cm ($n = 224$). We used PLS with simulated Landsat 7, Hyperion and WV-2 bands to predict biomass on this subset dataset, and then compared results to PLS results using the pooled dataset.

To test the ability to predict species-specific live biomass, we further ran species-specific models using square-root transformed above-ground biomass (g/m^2) in pure *S. acutus* plots and pure *Typha* spp. plots as response variables and simulated Hyperion bands as predictors. Pure *S. acutus* plots were those with 90% *S. acutus* biomass ($n = 135$), and pure *Typha* spp. plots were those with 90% *Typha* spp. biomass ($n = 247$) (**Table 3**). We additionally subset pure species plots by growing season period (May–June, July–August, September–October), to compare accuracy and error of models based on different phenological stages of plants.

2.5.2. Image-based models

Next, for each sensor type, we tested the relationships between field biomass and band reflectance from the corresponding satellite images. Multi-temporal datasets were possible for Landsat and WV-2 while a single date dataset was possible for Hyperion (**Table 2**). Band reflectance was extracted for each biomass plot based on plot location in ESRI ArcGIS 10.1. Image reflectance data was matched with biomass data temporally if the image date was no more than 7 days of biomass data collection. Early in the season during the stage of rapid growth, time between biomass data and image dates did not exceed two days. For 30 m Landsat 7 and Hyperion images, we averaged biomass from multiple plots within each pixel and used these averaged values for biomass estimation. These datasets were analyzed with PLS, as described in **Section 2.5.1**. Again, 20% of the data were withheld from model development and were used to validate the model.

2.5.3. Error reporting

For all models, we reported the explained variance (R^2), the RMSE (actual vs. predicted biomass measurements) of the validation dataset and the 95% confidence intervals of RMSE. We also reported the percent normalized RMSE (%RMSE) to compare field spectrometer-based and image-based model error, and models based on various subsets of these datasets. Because the units of predicted values were in square root biomass, we first transformed predictions and actual values in the validation dataset back to biomass before calculating RMSE and additional error terms. In addition, to test prediction accuracy for high biomass plots, for field spectrometer-based models we calculated RMSE and its 95% confidence intervals for those plots in the validation dataset with biomass values in the top 90th percentile, i.e., biomass $> 2500 \text{ g/m}^2$. The 95% confidence interval is calculated as (Eq. (1)) (Congalton & Green, 2009):

$$\text{CI} = \pm 1.96(S_{\text{RMSE}}), \quad \text{where } S_{\text{RMSE}} = \left(\sqrt{\sum (e - \text{RMSE})^2 / (n-1)} \right) / \sqrt{n}, \text{ and } e = y - y_{\text{hat}}. \quad (1)$$

Percent normalized RMSE is calculated as (Eq. (2)) (Ramoelo et al., 2013):

$$\% \text{RMSE} = [\text{RMSE} / (x_{\text{max}} - x_{\text{min}})] * 100. \quad (2)$$

2.6. Vegetation map

Because of their high spatial resolution, WV-2 images were selected to generate a vegetation map of the two study sites. To determine which pixels contained emergent vegetation, we used the Viper ENVI 4.7 plugin to conduct a multiple endmember spectral mixture analysis (MESMA) on September 2 and September 9, 2012 WV-2 images (Roberts et al., 1998). The sites were mapped according to the following classes: green *S. acutus*/*Typha* spp., litter, *Salix* sp., floating aquatic vegetation, and non-vegetated areas (open water, road). Field spectra collected for each endmember (**Section 2.2.1**) were used to train the classification. Attempts to map *S. acutus* and *Typha* spp. separately were unsuccessful. The land cover class was assigned using the highest endmember fraction for each pixel based on MESMA results.

Map accuracy was calculated using reference sites collected with a stratified random sampling design so that a minimum number of samples were selected from each stratum class (from 21 to 119 samples per class). Producer's accuracy and user's accuracy were calculated for each class, along with overall map accuracy and a kappa coefficient.

2.7. Biomass map

Biomass maps were generated for September 2 and September 9, 2012 WV-2 images, a September 12, 2012 Landsat 7 image, and the August 24 and August 26, 2012 Hyperion images using the sensor-specific PLS models (**Section 2.5.2**). Biomass was estimated only for those pixels classified as *S. acutus*/*Typha* spp. or litter in the WV-2 vegetation map. The WV-2 vegetation map was employed to produce biomass maps from the Landsat 7 and Hyperion images. The Landsat 7 and Hyperion images were resampled to 2 m and again only those pixels classified as *S. acutus*/*Typha* spp. or litter in the WV-2 vegetation map were used for biomass estimates. This resampling did not alter the spatial resolution of reflectance data from these images, but improved visualization of biomass by masking non-vegetated areas such as roads or open water from the final map. From each biomass map, average site-level biomass was estimated and compared to average site-level field measured biomass.

3. Results

3.1. Plot characteristics and measured biomass

Over two growing seasons, a total of 540 biomass plots were measured. The average biomass was 987.5 g/m^2 , with a range in plot biomass from 0 to 6335.7 g/m^2 . Based on outlier tests, the highest value was omitted from model runs; the highest biomass value in the modeled dataset was 5233.8 g/m^2 (**Table 1**). Seasonally, average biomass values ranged from 617.7 g/m^2 in May, to a peak of 1423.9 g/m^2 in July, down to 1014.5 g/m^2 in September, though maximum values were found in August. Biomass was on average much higher in the newly restored Sherman Island site (1834.1 g/m^2) compared to the Twitchell Island site (790.4 g/m^2).

Typha spp. plots were generally higher in biomass, with average biomass of 1138.5 g/m^2 compared to 770.6 g/m^2 for *S. acutus*. The low water plots ($< 15 \text{ cm}$ water depth) averaged 1037.3 g/m^2 and represented 46% of the total samples. The majority (58%) of the low water plots were pure *Typha* spp. plots. Sixty-five percent of *Typha* spp. plots were found in low water, compared to only 15% of *S. acutus* plots (**Table 3**).

In the study plots, substrate that contributed to background canopy reflectance was predominantly comprised of dead standing litter with

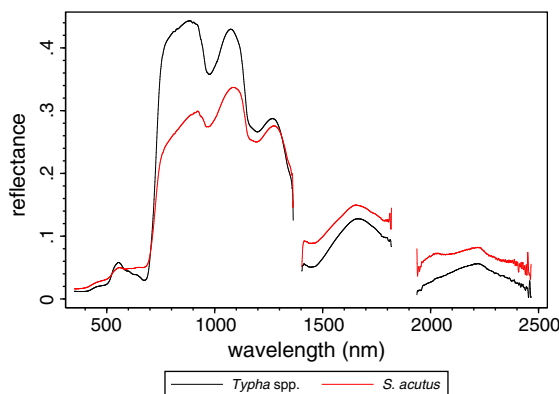


Fig. 3. Average mid-summer reflectance spectra for *Typha* spp. and *Schoenoplectus acutus* ($n = 10$ for each species).

some floating aquatic vegetation (Fig. 2). Most plots (350) did not contain any floating aquatic vegetation, though in 39 plots floating aquatic vegetation comprised over 50% of the plot area. Open water was minimally exposed, and so contributed minimally to overall canopy reflectance. Ninety percent of the plots were characterized by less than 10% cover of open water. Water depth ranged from 0 to 110 cm (Table 3).

3.2. Spectral signatures

Average peak biomass reflectance spectra of *Typha* spp. and *S. acutus* are provided in Fig. 3. These spectra represent an average of 10 pure plots of each species type collected in mid-summer (late July through August). As shown in this figure, *Typha* has a greater reflectance in the near infrared region of the spectrum, a steeper red-edge slope, greater absorption in the red region, and a higher peak in the green region than *S. acutus*. Both show strong water absorption features around 975 nm and 1250 nm and a small water absorption feature at 2260 nm, as well as a rise in the spectrum around 1518, a band sensitive to plant moisture (Thenkabail, Lyon, & Huete, 2012).

3.3. Field spectrometer-based models

The PLS regression of simulated Hyperion bands generated a lower RMSE ($560.9 \pm 152.7 \text{ g/m}^2$) than the regressions of simulated Landsat 7 or WV-2 bands (Table 4, Fig. 4) and a slightly higher R^2 value (0.46 for Hyperion compared to 0.40 and 0.39 for Landsat and

WV-2). Overlapping confidence intervals in the RMSE values for the simulated Hyperion, Landsat-7 and WV-2 models show that there was no significant difference in prediction accuracy among models. First order derivative Hyperion bands generated the highest RMSE ($590.2 \pm 158.8 \text{ g/m}^2$). Percent normalized RMSE for all four datasets were approximately 16%. For the high biomass, 90th percentile plots, %RMSE ranged from 79% to 82.3% depending on sensor type (Table 4).

3.3.1. Water inundation effects

The simulated first order derivative Hyperion bands were most successful in predicting biomass in the low-water inundation plots ($R^2 = 0.69$, RMSE = $419.2 \pm 157.5 \text{ g/m}^2$, %RMSE = 12.6%) (Table 4). The first order derivative Hyperion bands also performed the best for high biomass plots (RMSE of $622.7 \pm 183.2 \text{ g/m}^2$). Percent normalized RMSE in these plots was 49.8% compared to a range of 65.2% to 81.9% for the other datasets used to analyze low water plots.

3.3.2. Species-specific models

When the pure species plots were analyzed with simulated Hyperion bands, prediction of *Typha* spp. biomass was more successful than prediction of *S. acutus* biomass ($R^2 = 0.50$, %RMSE = 18.5%, compared to $R^2 = 0.15$, %RMSE = 24.9%) (Table 5). When plots were divided by season, *S. acutus* biomass was best predicted in the early summer months of May–June ($R^2 = 0.36$ compared to 0.02 and 0.06 for the July–August and September–October periods). In contrast, *Typha* spp. was best predicted late in the season with $R^2 = 0.71$ compared to 0.49 in mid-summer and 0.30 in early summer. Due to the greater success in predicting biomass of the pooled dataset of pure species plots and mixed species plots, and the challenge of generating species specific maps in these heterogeneous sites, we proceeded with generating maps based on models of the pooled datasets.

3.3.3. Loadings

For the simulated Hyperion dataset, bands with the highest negative loadings in component one were found in the shortwave infrared region of the spectrum, particularly around 1750 and 2000 nm with the most negative values at 2002, 2012, 2022, 2032 and 1790 nm (Fig. 5). High positive loadings were found in the near infrared region among bands ranging from 800 to 900 nm, with the highest loadings at 823, 854, 803 and 844 nm. For component two, important bands were those in the near infrared section, ranging from 850 to 1100 nm, with the highest values found at 884, 894, 874, 1073, and 905 nm. Bands with the highest loadings in the first component in the first order derivative Hyperion

Table 4

Summary statistics for partial least squares regression of aboveground biomass (g/m^2) with simulated Hyperion, Hyperion first derivative reflectance, Landsat 7 and World View-2 bands, all derived from field spectrometer reflectance data. a) Pooled plot data, b) vegetation plots where water inundation was less than 15 cm.

A. All plots	Hyperion	Hyperion 1stdv.	Landsat 7	World View-2
# components	7	1	1	3
RMSE ($\pm 95\%$ CI)	560.9 (408.2 713.6)	590.2 (431.4 749.0)	570.3 (416.6 724.1)	573.5 (418.7 728.2)
%RMSE	15.7%	16.6%	16.0%	16.1%
RMSE, 90th pct. ($\pm 95\%$ CI)	1172.3 (734.6 1609.9)	1219.1 (798.5 1639.7)	1194.7 (850.8 1538.7)	1170.8 (796.1 1545.6)
%RMSE, 90th pct.	79.1%	82.3%	80.6%	79.0%
R^2	0.46	0.42	0.40	0.39
B. Low water plots	Hyperion	Hyperion 1 stdv.	Landsat 7	World View-2
# components	1	3	1	3
RMSE ($\pm 95\%$ CI)	533.7 (337.5 729.9)	419.2 (261.7 576.6)	518.6 (325.6 711.5)	469.2 (292.0 646.4)
%RMSE	16.0%	12.6%	15.5%	14.1%
RMSE, 90th pct. ($\pm 95\%$ CI)	1024.3 (742.2 1306.4)	622.7 (439.5 806.0)	973.2 (693.1 1253.2)	815.7 (502.5 1128.9)
%RMSE, 90th pct.	81.9%	49.8%	77.8%	65.2%
R^2	0.57	0.69	0.60	0.61

RMSE = root mean square error of predictions from validation dataset in g/m^2 , plus 95% confidence intervals for RMSE.

RMSE, 90th pct. = RMSE for validation samples in the 90th percentile of biomass values.

%RMSE = percent normalized RMSE [$\text{RMSE}/(\bar{x}_{\max} - \bar{x}_{\min})^* 100$].

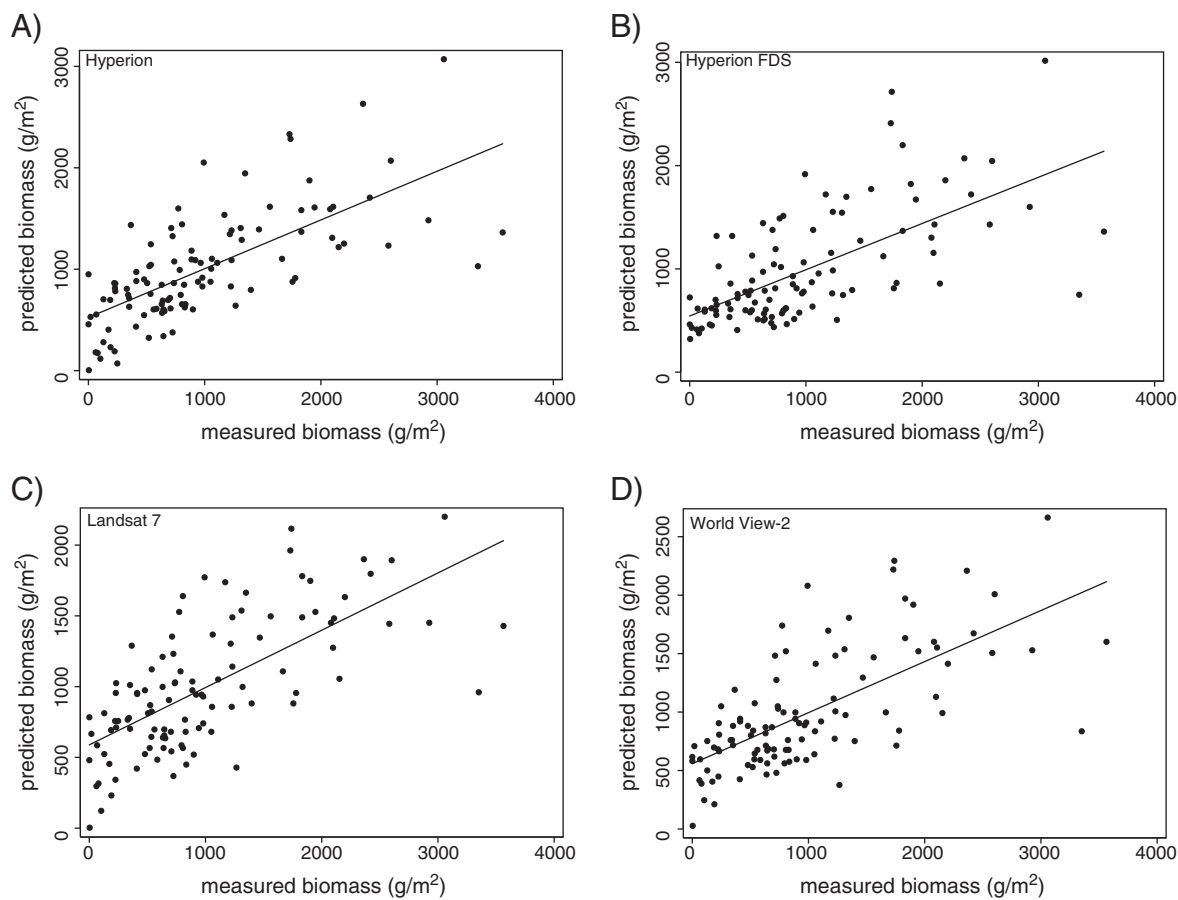


Fig. 4. Plots of predicted to observed biomass in validation datasets based on partial least squares regression of aboveground biomass with simulated A) Hyperion, B) Hyperion first derivative reflectance, C) Landsat 7 and D) World View-2 bands derived from field spectrometer reflectance data.

dataset were 732, 721, 742 and 711 nm. Negative peaks were found at 1144, 1134, 1124, 952 and 932 nm. In component two, important negative peaks were at 1013, 701, 711, 691 and 721 nm. Positive loading values were at 2254, 2244 and 2234 nm. Loading values from the simulated Landsat 7 and WV-2 datasets reflect a similar pattern found with the hyperspectral bands. For both of these datasets, bands in the near infrared have high loading values (Landsat 7 band 4 and WV-2 bands 7 and 8). Landsat 7 bands 5 and 7 in the shortwave infrared also have highly negative loading values.

3.4. Image-based models

The multi-temporal dataset generated with the Landsat 7 satellite scenes predicted biomass slightly better than the dataset generated by

the WV-2 images ($R^2 = .56$, %RMSE = 20.9%, compared to $R^2 = .45$, %RMSE = 21.5%). The Hyperion dataset was the least successful in predicting biomass ($R^2 = .27$, %RMSE = 33.5%) (Table 6, Fig. 6).

3.5. The biomass maps

The overall accuracy of the MESMA-based vegetation cover map of the two study sites was 96%. The emergent vegetation and plant litter was mapped with high accuracy (91.6% and 100% producer's accuracy, respectively and 100% and 88% user's accuracy, respectively) (Table 7). In cases of misclassification, plant litter was confused with emergent vegetation.

In the mid-August–early September time period when images were acquired, average field-measured biomass at Sherman Island was far

Table 5
Summary statistics for partial least squares regression of aboveground biomass (g/m²) for pure species plots by season with simulated Hyperion bands derived from field spectrometer reflectance data. A. *S. acutus* plots, B. *Typha* spp. plots.

A. <i>S. acutus</i>	all plots	May–June	July–Aug.	Sept.–Oct.
# components	3	1	1	1
RMSE ($\pm 95\%$ CI)	453.5 (206.9 700.1)	255.8 (68.6 443.0)	453.4 (130.1 776.7)	609.1 (140.5 1077.7)
%RMSE	24.9%	26.6%	30.0%	34.3%
R^2	0.15	0.36	0.02	0.06
B. <i>Typha</i> spp.				
# components	1	1	3	5
RMSE ($\pm 95\%$ CI)	601.3 (362.5 840.1)	252.5 (79.9 425.1)	724.6 (320.4 1128.8)	516.5 (234.7 798.3)
%RMSE	18.5%	24.0%	23.1%	21.0%
R^2	0.50	0.30	0.49	0.71

RMSE = root mean square error of predictions from test dataset in g/m², plus 95% confidence intervals for RMSE.

%RMSE = percent normalized RMSE [RMSE/(x_{max} – x_{min}) * 100].

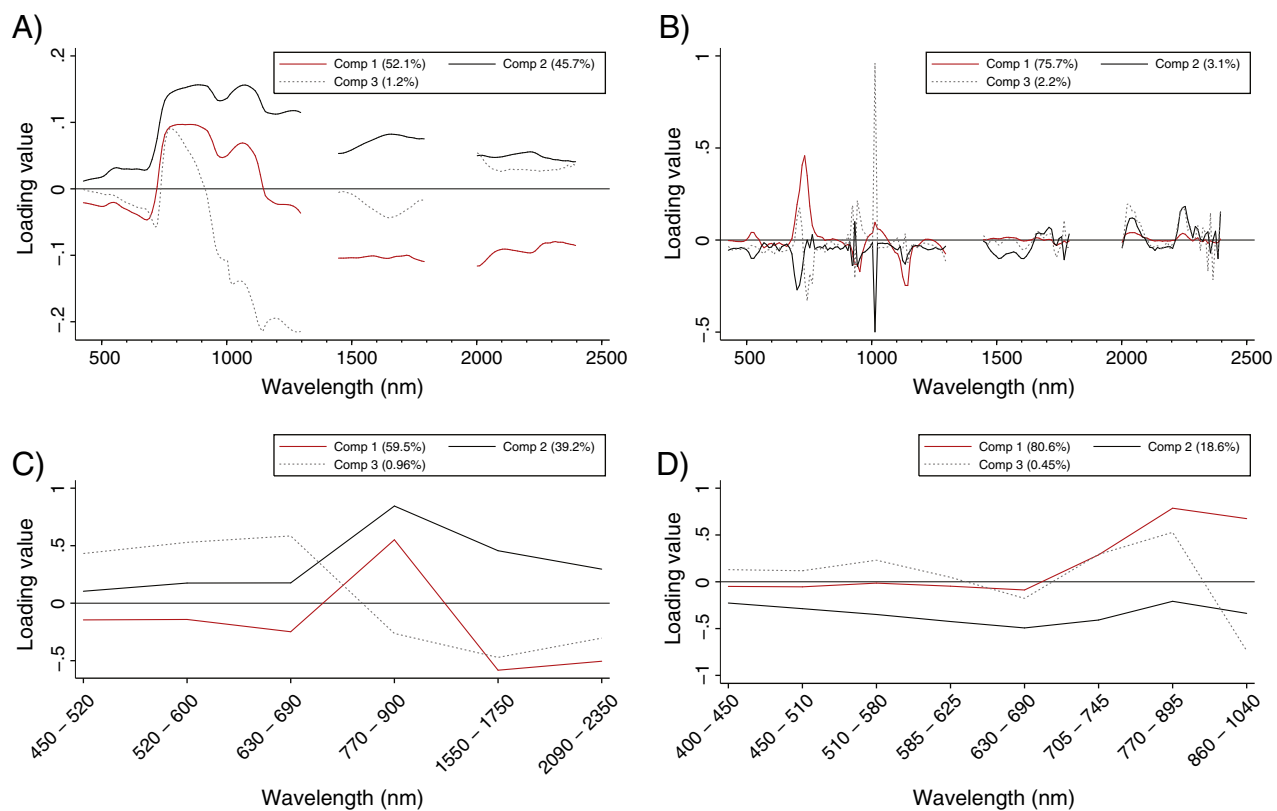


Fig. 5. Loadings of the first three partial least squares factors plotted against wavelength, excluding wavelength regions associated with strong water absorption features for partial least squares regression of aboveground biomass with simulated A) Hyperion, B) Hyperion first derivative reflectance, C) Landsat 7 and D) World View-2 bands derived from field spectrometer reflectance data. The percent variability in measured biomass captured in each component is provided for each plot.

greater than at Twitchell Island, with a mean of 2303 g/m² compared to a mean of 1357 g/m² (Table 8). The WV-2 and Landsat 7 biomass maps reflect this difference in biomass between sites (Fig. 7). At Sherman Island, the average biomass from the Landsat 7 map was 1977 g/m² and the WV-2 biomass average was 3004 g/m², compared to Twitchell Island, where averages were 1141 g/m² and 1274 g/m², respectively. At Twitchell Island, the site-averaged biomass from all image types was within 216 g/m² of the field-based site-averaged biomass (Table 8). In contrast the Hyperion biomass map underestimates biomass at the Sherman Island site, and the WV-2 image provides an overestimate, compared to the field-measured biomass average in mid-August (Fig. 7, Table 8).

4. Discussion

This study's efforts to predict aboveground biomass of emergent wetland vegetation with simulated satellite bands from field spectrometer data demonstrate that the use of narrow bands improved predictions somewhat, but not significantly more than the use of broad bands. These results are based on a comparison of RMSE and its 95% confidence intervals for the validation dataset as well as the subset of validation samples with biomass values in the 90th percentile

(Table 4). The large confidence intervals around RMSE reflect the wide range in the residuals calculated from predicted and actual biomass values in both the hyperspectral and multispectral datasets. Biomass models based on first derivative reflectance hyperspectral bands predicted biomass substantially better in low inundation plots, with a drop in %RMSE to 12.6%. While *Typha* spp. models predicted biomass better than *S. acutus* models, the pooled dataset including mixed species plots performed better than species-specific models. In comparison, PLS models based on multispectral satellite images predicted biomass more accurately than a model based on a single hyperspectral satellite image, though the large confidence intervals around the RMSE for each model do not indicate a statistically significant difference in average error across models. While sensor features and satellite revisit times likely influenced model error, environmental conditions and plant community structure also likely controlled biomass prediction.

4.1. Water inundation effects

Our results show that similar to past studies, water depth was related to accuracy in estimates of biophysical characteristics of vegetation. Others found that water inundation affects the red edge position of spectra and reduces the near infrared reflectance at 900 to 1100 nm

Table 6

Summary statistics for partial least squares regression of mixed species aboveground biomass (g/m²) with reflectance data from Hyperion, Landsat 7 and World View-2 images.

	Hyperion	Landsat 7	World View-2
# components	1	1	2
RMSE ($\pm 95\%$ CI)	620.9 (0.0 1322.9)	556.5 (69.3 1043.8)	659.7 (307.1 1012.2)
%RMSE	33.5%	20.9%	21.5%
R ²	0.27	0.56	0.45

RMSE = root mean square error of predictions from test dataset in g/m², plus 95% confidence intervals for RMSE.

%RMSE = percent normalized RMSE [RMSE/(x_{max} – x_{min}) * 100].

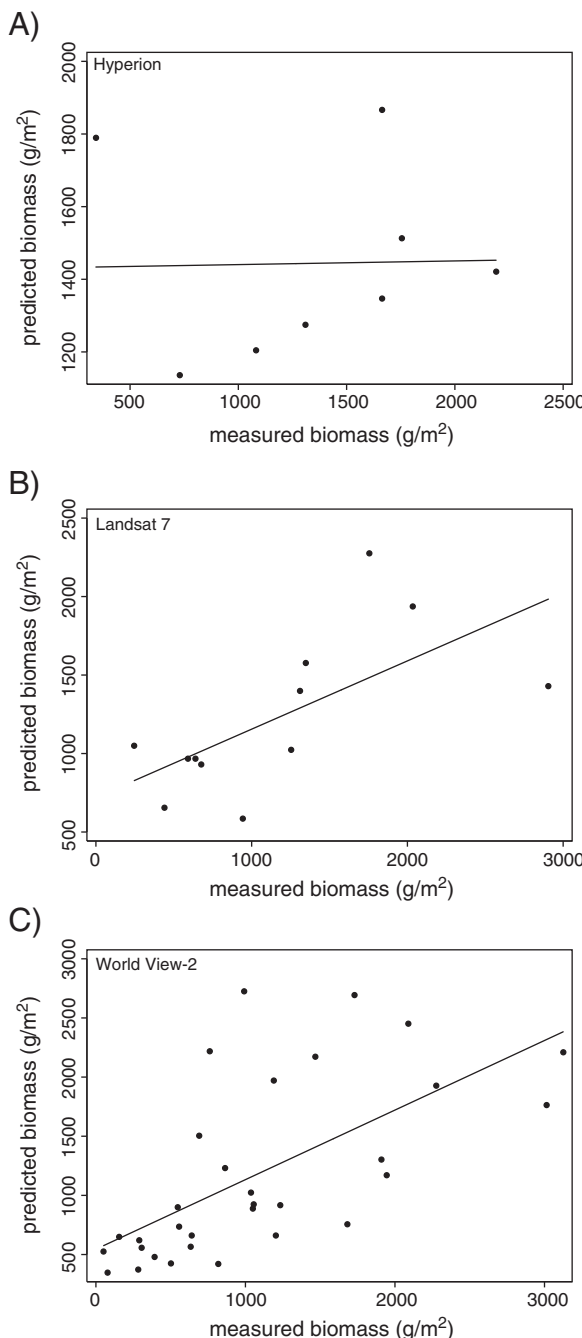


Fig. 6. Plots of predicted to observed biomass in validation datasets based on partial least squares regression of aboveground biomass with reflectance data from A) Hyperion, B) Landsat 7 and C) World View-2 satellite images.

(Beget & Di Bella, 2007; Kearney et al., 2009; Turpie, 2013). The degree of change in the near infrared spectrum is related to canopy structure and background reflectance; a more rapid reduction in NIR with increasing water depth is more likely for erectophile species with low leaf area (e.g. *S. acutus*), since the substrates of these canopies are more readily visible in nadir views. In contrast substrate is more hidden by the canopy of plants with broad leaves, more horizontal leaf orientation and higher leaf area (e.g. *Typha* spp.), and the declines in the NIR reflectance are far less dramatic (Kearney et al., 2009). As seen in the loading plots (Fig. 5), the shortwave infrared region was important in the final models. The effects of water inundation on this region of the spectrum are unclear, and a more controlled experimental study to identify any potential effects is needed.

In some cases vegetation was inundated in over 1 m of water. In these cases approximately half or more of the plant was under water and the water surface was on average approximately one meter from the top of the canopy. Plots with deep water were generally found at the mature Twitchell Island wetland, where boardwalks allowed access to deep water areas. In these deep water plots, open water was almost always covered with litter and floating aquatic vegetation. Thus litter and floating aquatics were the dominant background surface cover influencing standing biomass reflectance. One confounding factor was that most low water plots were dominated by *Typha* spp. (Table 3); low water habitat and a broadleaf structure likely aided development of accurate *Typha* spp. biomass models.

4.2. Species-specific models

Efforts to develop species-specific biomass models indicated that it is much more feasible to predict biomass of *Typha* spp. than of *S. acutus*, though the overall RMSE of the validation datasets were lower for the pooled dataset compared to any species-specific model. The sample size of the *Typha* spp. dataset was larger than the *S. acutus* dataset (247 vs. 135), which may have contributed to the lower RMSE for *Typha* spp. models. However, PLS of a subset of 135 random *Typha* spp. plots resulted in the same validation RMSE as the full *Typha* spp. model (RMSE = 601.4 g).

Challenges in predicting *S. acutus* biomass are likely related to its structure, phenology, and environmental setting. Both species show steep slopes in the NIR reflectance from 740 to 940 nm (Fig. 3), common for erectophile plants (Thenkabail, Smith, & De Pauw, 2002). However the pigments and structure of *S. acutus* influence its spectral signature, and create differences in its signature compared to that of *Typha* spp. *S. acutus* produces a lower green peak compared to *Typha*. The vertical structure of the stem, and lack of visible horizontal leaves in the canopy allow more light to penetrate the canopy, producing a lower reflectance in the near infrared wavelengths (Mutanga & Skidmore, 2004; Ollinger, 2011). The higher reflectance in the visible wavelengths for *S. acutus* may also be caused by the quantity of dead standing vegetation that co-occurs with this species in the Twitchell Island site (Fig. 2), and the litter's greater contribution to plot reflectance, as little canopy cover

Table 7
Accuracy assessment of vegetation mapping for Twitchell Island and Sherman Island wetland sites.

Reference data		Floating aquatic vegetation	Non-vegetated	Salix sp.	Plant litter	<i>Typha</i> spp./ <i>S. acutus</i>	Total	User's accuracy
Map Data	Floating aquatic vegetation	49		3		2	54	90.7%
	Non-vegetated	101					101	100.0%
	<i>Salix</i> sp.	1		18		1	20	90.0%
	Plant litter				50	7	57	87.7%
	<i>Typha</i> spp./ <i>S. acutus</i>	109	109	100.0%				
	Total	50	101	21	50	119	341	
	Producers accuracy	98.0%		100.0%	85.7%	100.0%	91.6%	
	Overall accuracy	95.9%						
	Kappa coefficient	0.99						

Table 8

Site-averaged aboveground biomass (g/m^2) based on field measurements and image-based estimates for Hyperion, Landsat 7 and World View-2 images, for A. Twitchell Island and B. Sherman Island sites. N = number of field samples or number of pixels in biomass maps.

A. Twitchell Island	n	Mean (g/m^2)
Measured biomass, 9/7/12	37	1357
Hyperion	12,857	1419
Landsat 7	12,857	1141
World View-2	12,857	1274
B. Sherman Island	n	Mean (g/m^2)
Measured biomass, 8/15/12	37	2303
Hyperion	97,379	1103
Landsat 7	89,598	1977
World View-2	97,379	3004

exists to mask it. In addition, by mid-summer *S. acutus* stems begin to brown at the top, which may also lead to high reflectance in the visible wavelengths and mask vigorous green vegetation below browned tips. Similar results were found by Langley and Megonigal (2012) when they used spectral reflectance to estimate biomass of *Schoenoplectus americanus*, another species consisting of single vertical stems.

4.3. Sources of error in models and maps

Multiple sources of error contribute to the challenges of mapping biomass in these heterogeneous restored wetlands, including field measurements, allometric estimates of biomass, errors around scaling biomass estimates and spatial and temporal plot co-location errors (Asner et al., 2013). First, while the allometric equations used to estimate biomass in the small measured plots were well tested and had

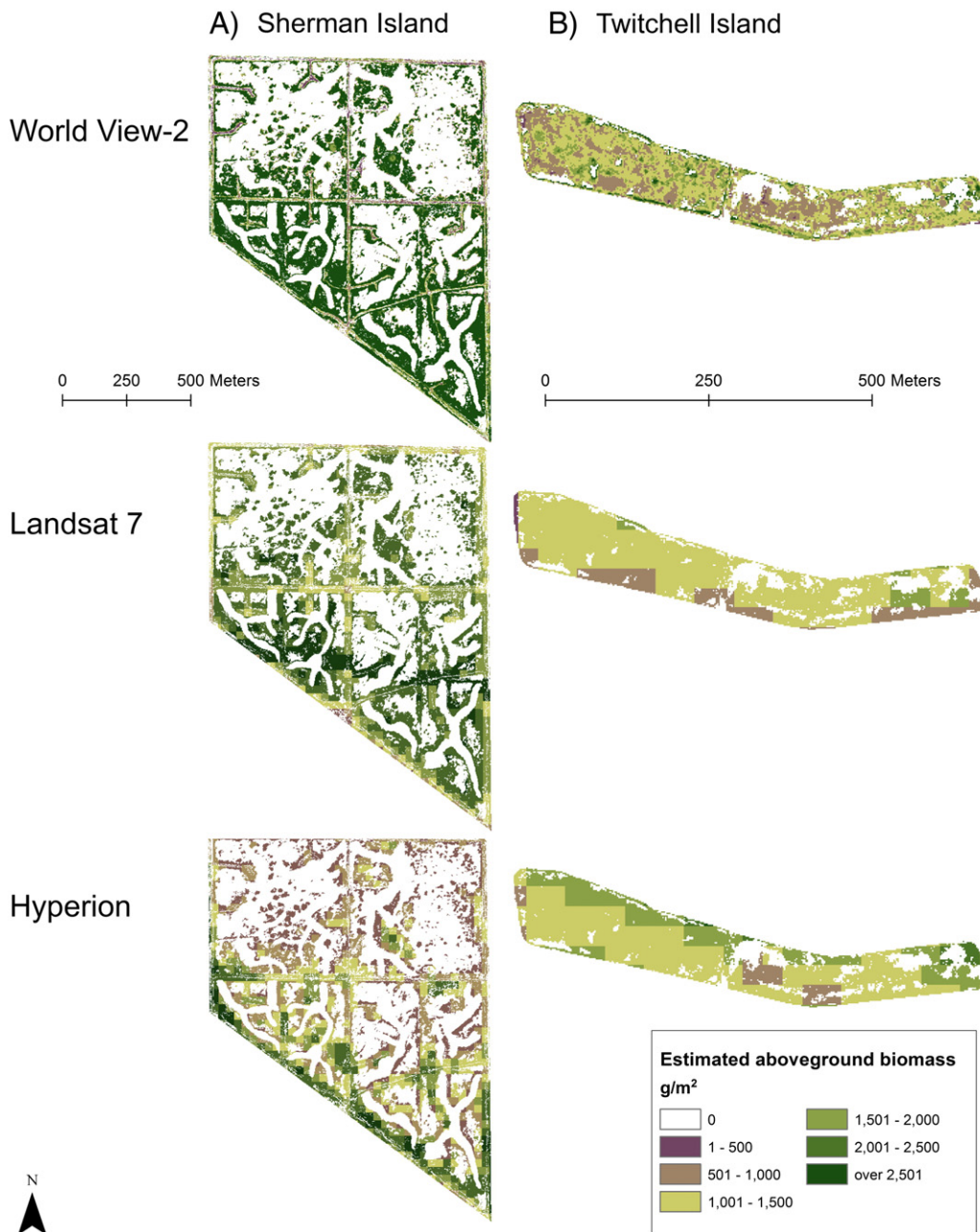


Fig. 7. Maps of estimated biomass for late-summer Hyperion, Landsat 7, and World View-2 images for A) Sherman Island and B) Twitchell Island. Biomass was mapped for pixels classified as emergent marsh vegetation (*Typha* spp. and/or *S. acutus*) or plant litter.

high explanatory power, there is error associated with these measurements. Second, biomass was measured in small 0.1 m² plots, and scaled up to 1 m² plots, which assumes consistency in percent cover and species composition at the two scales. The field of view of the field spectrometer was calculated to be 1.8 m, and the satellite pixel resolutions ranged from 2 to 30 m. In all cases, we assumed that measured biomass was representative of biomass of the whole pixel. More stratified sampling across pixels would have improved models, though site access made a stratified sampling scheme, especially with the use of the field spectrometer, challenging. Some positional error also exists with the georeferencing of WV-2 imagery. The high spatial resolution created challenges for precise registration with plots, and high heterogeneity of sites generates noise across adjacent pixels (Lu, 2006), so that high variation in reflectance was common. In addition, for the image-based models, biomass was not collected on the date of image, though only biomass measurements taken within a week of image acquisition were used. However this temporal difference between image acquisition and field measurements could create a discrepancy between field reflectance and measured biomass.

The analysis of field spectrometer data showed that prediction errors were substantially higher for high biomass plots greater than 2500 g/m², compared to average error for the pooled datasets. While RMSE of the 90th percentile plots was similar for both simulated narrowband and broadband datasets, the dynamic range of the predicted values was greater for the narrowband datasets (maximum of 3000 g/m² for the simulated Hyperion and Hyperion first order derivative datasets) and lower for the broadband datasets (maximum of 2200 g/m² for Landsat 7 and maximum of 2665 g/m² for WV-2). These results are suggestive of other studies that show multiple hyperspectral bands help to reduce the problem of saturation (Chen et al., 2009; Mutanga & Skidmore, 2004; Thenkabail et al., 2000). However we expected a greater reduction in prediction error with the hyperspectral data than was observed in our study.

Ultimately we chose to map estimated biomass using a mixed species model due to its higher accuracy and also because of difficulty in mapping individual species using the MESMA approach. Better results may have been achieved with object based remote sensing and high resolution satellite imagery, which has shown promise in distinguishing the two species (Tuxen et al., 2011). However at our sites, especially at Twitchell Island, the two species were highly intermixed, and even with high resolution WV-2 pixels, there are few regions that are dominated by a single species.

At the site level, all image-based biomass estimates for Twitchell Island were relatively similar. Average biomass estimated from Landsat 7 was closest to average field-measured biomass for Sherman Island. Overestimates of biomass from the WV-2 images at Sherman Island were in contrast to past results that showed more accurate biomass predictions with this sensor (Mutanga et al., 2012). The model prediction errors for WV-2 and Landsat 7 were somewhat lower than Hyperion model errors, though not statistically lower based on RMSE confidence intervals. Lower model errors for WV-2 and Landsat may have resulted because models were constructed from a multi-temporal dataset generated from satellite images collected over the growing season. This larger dataset allowed for the inclusion of a wider dynamic range in biomass values, and incorporation of phenological variation in plant growth and structure. Only one Hyperion image was acquired, and though its timing corresponded with peak biomass and it contained multiple spectral bands, model development was poor since fewer field samples were collected around the time of image acquisition.

Landsat 7 and Hyperion scenes were downscaled to the same resolution as WV-2 to improve the visualization of biomass in maps produced with these images. However even though biomass estimation was applied to downsampled Landsat 7 or Hyperion pixels, image band information applied to these pixels were from the original 30 m pixels. We only used pixels that were fully contained in the wetland because pixels on the edge still contained a mixed signal from vegetation plus

surrounding features such as roads and levees. This edge effect was particularly problematic for the Twitchell Island wetland, due to its small size and narrow shape. This effect is evident in the Landsat 7 biomass map of this site, where low biomass is indicated along the southern edge, where the wetland abuts a dirt road.

4.4. Comparison of sensor attributes

The Sacramento–San Joaquin River Delta, where our sites were located, is one of the most significantly modified deltas in the world. The area of remaining wetlands is only 3% of its former extent (1.9% of the Delta area), and these wetlands are highly disturbed, fragmented or disconnected from other habitat types (Whipple et al., 2012). Now most emergent wetlands are limited to small in-channel islands in the San Joaquin River or exist as thin strips along the margins of artificial levees (Whipple et al., 2012).

A very high percentage (up to 87% recorded in one survey) of natural resource managers use one or many types of geospatial technologies to collect, visualize, integrate or interpret their information about natural resources (Selvarajan, Mohamed, White, & Boodram, 2009). The type of technology, including the choice of satellite sensor data, is a factor of acquisition cost, labor required for processing as well as the level of error associated with its use (Lewis, Phinn, & Arroyo, 2013; Lu, 2006). When investigating within site variability across biomass maps, it is clear that the high spatial resolution of WV-2 allows for the discernment of spatial variability in biomass. Such biomass variability was most evident within the Twitchell Island impoundments, where patches of litter established in the mature marsh, producing a more defined mosaic of high and low biomass plots. In comparison, vegetation within the Sherman Island impoundment was more uniformly green. High spatial detail may be desirable for wetland managers in the Sacramento–San Joaquin River Delta and elsewhere in the Western U.S., when wetlands are small, fragmented, and heterogeneous (Phinn, 1998; Phinn et al., 1996).

While high resolution commercial satellite imagery may provide accurate biomass estimation at a local scale, use at the regional scale becomes challenging because of the storage capacity needed for a large volume of data, the expense to purchase the images, and the time and labor needed to process images. In addition, current lack of shortwave infrared bands in most commercial imagery may create difficulty in developing biomass models (Lu, 2006). In our study we found that shortwave infrared bands are beneficial for biomass mapping, based on their high loading values in the field spectrometer based-Hyperion and Landsat 7 models (Fig. 5).

Landsat data has become a main source of biomass estimation at local and regional scales. This medium spatial-resolution data provides more potential for biomass mapping at a regional level, but mixed pixels and data saturation can be a problem in those sites with complex biophysical environments (Lu, 2006). Improvements to biomass mapping are possible with the new Landsat 8 satellite data that became available May 2013, which have improved 12-bit quantization, compared to 8-bit on the older Landsat sensors. Additional opportunities will come with the Hyperspectral Infrared Imager or HyspIRI satellite, which will have a spatial resolution of 60 m. HyspIRI will include an imaging spectrometer measuring from the visible to short wave infrared wavelengths in 10 nm contiguous bands, as well as a multispectral imager measuring from 3 to 12 μm in the mid and thermal infrared wavelengths (<http://hyspiri.jpl.nasa.gov/>). In addition Digital Globe plans to launch World View-3 in 2014, which will have eight shortwave infrared bands at 3.7 m resolution (<http://www.digitalglobe.com/about-us/content-collection#worldview-3>).

5. Conclusion

A comparison of models of freshwater emergent vegetation biomass shows that narrowband reflectance data can predict biomass somewhat,

though not significantly better than broadband reflectance data. Hyperspectral first derivative reflectance spectra best predicted biomass for plots where water levels were less than 15 cm. The use of PLS for this analysis did not substantially remove the saturation effects common when using vegetation indices for biomass estimation and did not eliminate the effect of water inundation on model accuracy. Mixed-species models of biomass performed better than species-specific models. Image-based models of biomass from a multi-temporal Landsat 7 dataset performed better at the pixel and site scale than models generated from WV-2 or Hyperion datasets. A high return frequency of satellite sensors may be desirable for generating a robust model of biomass for these sites, as a multi-temporal dataset can capture a greater range in plant growth. While shortwave infrared reflectance data aids biomass prediction, managers need to consider the tradeoffs between cost, additional spectral information at these wavelengths and the high spatial resolution of most commercial satellite imagery, which can identify within-site variability for the small, fragmented marshes common to the Sacramento–San Joaquin River Delta and elsewhere.

Acknowledgments

This research was supported by K. Byrd's NASA New Investigator Program in Earth Sciences Grant Number: NNN10A086I and the USGS Land Change Science Program. We thank Susan Stitt and Carol Mladinich, USGS Geosciences and Environmental Change Science Center, for loan of the ASD field spectrometer. We thank Samuel Blanchard, Sophie Kolding, Feng Zhao, Lisa Schile, Scott Lydon, Adam McClure, and Lisamarie Windham-Myers for field and logistical help. We thank Prasad Thenkabail for assistance with project planning. We thank Robin Miller for the development of the biomass allometric equations used in this study. Finally we thank Iryna Dronova and three anonymous reviewers for review of this manuscript.

Any use of trade, firm, or product names is for descriptive purposes only and does not imply endorsement by the U.S. Government.

References

- Asner, G., Mascaro, J., Anderson, C., Knapp, D., Martin, R., Kennedy-Bowdoin, T., et al. (2013). High-fidelity national carbon mapping for resource management and REDD+. *Carbon Balance and Management*, 8, 7.
- Barbour, M. G., Burk, J. H., Pitts, W. D., Gilliam, F. S., & Schwartz, M. W. (1999). *Terrestrial plant ecology*. Menlo Park: Benjamin/Cummings.
- Beget, M. E., & Di Bella, C. M. (2007). Flooding: The effect of water depth on the spectral response of grass canopies. *Journal of Hydrology*, 335, 285–294.
- Bellucci, E., Camuffo, M., Ferrari, S., Modenese, L., Silvestri, S., Marani, A., et al. (2006). Mapping salt-marsh vegetation by multispectral and hyperspectral remote sensing. *Remote Sensing of Environment*, 105, 54–67.
- Bridgman, S. D., Megonigal, J. P., Keller, J. K., Bliss, N. B., & Trettin, C. (2006). The carbon balance of North American wetlands. *Wetlands*, 26, 889–916.
- Chen, J., Gu, S., Shen, M., Tang, Y., & Matsushita, B. (2009). Estimating aboveground biomass of grassland having a high canopy cover: An exploratory analysis of in situ hyperspectral data. *International Journal of Remote Sensing*, 30, 6497–6517.
- Congalton, R. G., & Green, K. (2009). *Assessing the accuracy of remotely sensed data: principles and practices* (2nd ed.). Boca Raton: CRC Press, Taylor and Francis Group.
- Crooks, S., Emmett-Mattox, S., & Findsen, J. (2010). *Findings of the National Blue Ribbon Panel on the development of a greenhouse gas offset protocol for tidal wetlands restoration and management: Action plan to guide protocol development*. 15 pp. Restore America's Estuaries, Philip Williams & Associates, Ltd., and Science Applications International Corporation (<https://www.estuaries.org/images/stories/rae-action-plan-tidal-wetlandsghg-offset-protocol-aug-2010.pdf>). Date accessed: 1 August 2011).
- Dadon, A., Ben-Dor, E., & Karnieli, A. (2010). Use of derivative calculations and minimum noise fraction transform for detecting and correcting the spectral curvature effect (smile) in Hyperion images. *IEEE Transactions on Geoscience and Remote Sensing*, 48, 2603–2612.
- Dawson, T. P., & Curran, P. J. (1998). Technical note. A new technique for interpolating the reflectance red edge position. *International Journal of Remote Sensing*, 19, 2133–2139.
- Deegan, L. A., Johnson, D. S., Warren, R. S., Peterson, B. J., Fleeger, J. W., Fagherazzi, S., et al. (2012). Coastal eutrophication as a driver of salt marsh loss. *Nature*, 490, 388–392.
- de Jong, S. M. (1998). Imaging spectrometry for monitoring tree damage caused by volcanic activity in the Long Valley caldera, California. *ITC Journal*, 1, 1–10.
- Demetriades-Shah, T. H., Steven, M. D., & Clark, J. A. (1990). High resolution derivative spectra in remote sensing. *Remote Sensing of Environment*, 33, 55–64.
- Deverel, S. J., & Leighton, D. A. (2010). Historic, recent, and future subsidence, Sacramento–San Joaquin Delta, California, USA. *San Francisco Estuary and Watershed Science*, 8, 23.
- Emmett-Mattox, S., Crooks, S., & Findsen, J. (2011). Grasses and gases. *The Environmental Forum*, 28, 30–35.
- Geladi, P., & Kowalski, B. R. (1986). Partial least-squares regression: A tutorial. *Analytica Chimica Acta*, 185, 1–17.
- Goetz, S., & Dubayah, R. (2011). Advances in remote sensing technology and implications for measuring and monitoring forest carbon stocks and change. *Carbon Management*, 2, 231–244.
- Gorham, E., Lehman, C., Dyke, A., Clymo, D., & Janssens, J. (2012). Long-term carbon sequestration in North American peatlands. *Quaternary Science Reviews*, 58, 77–82.
- Gross, M. F., Hardisky, M. A., Klemas, V., & Wolf, P. L. (1987). Quantification of biomass of the marsh grass *Spartina alterniflora* loisel using Landsat Thematic Mapper imagery. *Photogrammetric Engineering and Remote Sensing*, 53, 1577–1583.
- Gross, M. F., Hardisky, M. A., Wolf, P. L., & Klemas, V. (1993). Relationships among *Typha* biomass, pore water methane, and reflectance in a Delaware (USA) brackish marsh. *Journal of Coastal Research*, 9, 339–355.
- Hansen, P. M., & Schjoerring, J. K. (2003). Reflectance measurement of canopy biomass and nitrogen status in wheat crops using normalized difference vegetation indices and partial least squares regression. *Remote Sensing of Environment*, 86, 542–553.
- Hardisky, M. A., Daiber, F. C., Roman, C. T., & Klemas, V. (1984). Remote sensing of biomass and annual net aerial primary productivity of a salt marsh. *Remote Sensing of Environment*, 16, 91–106.
- Hardisky, M. A., Klemas, V., & Michael Smart, R. (1983). The influence of soil salinity, growth form, and leaf moisture on the spectral radiance of *Spartina alterniflora* canopies. *Photogrammetric Engineering and Remote Sensing*, 49, 77–83.
- Hardisky, M. A., Michael Smart, R., & Klemas, V. (1983). Growth response and spectral characteristics of a short *Spartina alterniflora* salt marsh irrigated with freshwater and sewage effluent. *Remote Sensing of Environment*, 13, 57–67.
- Hopkinson, C. S., Cai, W. J., & Hu, X. (2012). Carbon sequestration in wetland dominated coastal systems – A global sink of rapidly diminishing magnitude. *Current Opinion in Environmental Sustainability*, 4, 186–194.
- ITT Visual Information Solutions (2009). *Atmospheric correction module: QUAC and FLASH user's guide version 4.7*.
- Jensen, J. R. (1998). Extraction of smooth cordgrass biomass and leaf area index parameters from high resolution imagery. *Geocarto International*, 13, 25–34.
- Jensen, J. R. (2002). Remote sensing of biomass, leaf area index, and chlorophyll and content in the ACE Basin National Estuarine Research Reserve using sub meter digital camera imagery. *Geocarto International*, 17, 27–36.
- Kayranli, B., Scholz, M., Mustafa, A., & Hedmark, A. (2010). Carbon storage and fluxes within freshwater wetlands: A critical review. *Wetlands*, 30, 111–124.
- Kearney, M. S., Stutzer, D., Turpie, K., & Stevenson, J. C. (2009). The effects of tidal inundation on the reflectance characteristics of coastal marsh vegetation. *Journal of Coastal Research*, 25, 1177–1186.
- Klemas, V. (2013). Remote sensing of coastal wetland biomass: An overview. *Journal of Coastal Research*, 29, 1016–1028.
- Kochubey, S. M., & Kazantsev, T. A. (2012). Derivative vegetation indices as a new approach in remote sensing of vegetation. *Frontiers of Earth Science*, 6, 188–195.
- Langley, J. A., & Megonigal, J. P. (2012). Field-based radiometry to estimate tidal marsh plant growth in response to elevated CO₂ and nitrogen addition. *Wetlands*, 32, 571–578.
- Lewis, D., Phinn, S., & Arroyo, L. (2013). Cost-effectiveness of seven approaches to map vegetation communities – A case study from Northern Australia's tropical savannas. *Remote Sensing*, 5, 377–414.
- Lu, D. (2006). The potential and challenge of remote sensing-based biomass estimation. *International Journal of Remote Sensing*, 27, 1297–1328.
- Masek, J. G., Vermote, E. F., Saleous, N. E., Wolfe, R., Hall, F. G., Huemmrich, K. F., et al. (2006). A Landsat surface reflectance dataset for North America, 1990–2000. *IEEE Geoscience and Remote Sensing Letters*, 3, 68–72.
- Masek, J. G., Vermote, E. F., Saleous, N., Wolfe, R., Hall, F. G., Huemmrich, F., et al. (2013). LEDAPS calibration, reflectance, atmospheric correction preprocessing code, version 2. Model product (Available on-line [<http://daac.ornl.gov>] from Oak Ridge National Laboratory Distributed Active Archive Center, Oak Ridge, Tennessee, U.S.A.).
- McLeod, E., Chmura, G. L., Bouillon, S., Salm, R., Björk, M., Duarte, C. M., et al. (2011). A blueprint for blue carbon: Toward an improved understanding of the role of vegetated coastal habitats in sequestering CO₂. *Frontiers in Ecology and the Environment*, 9, 552–560.
- Mevik, B. H., & Cedervist, H. R. (2004). Mean squared error of prediction (MSEP) estimates for principal component regression (PCR) and partial least squares regression (PLSR). *Journal of Chemometrics*, 18, 422–429.
- Mevik, B. H., & Wehrens, R. (2007). The pls package: Principle component and partial least-squares regression in R. *Journal of Statistical Software*, 18, 1–24.
- Miller, R. L., Fram, M. S., Fujii, R., & Wheeler, G. (2008). Subsidence reversal in a re-established wetland in the Sacramento–San Joaquin Delta, California, USA. *San Francisco Estuary and Watershed Science*, 6, 1–20.
- Miller, R. L., & Fujii, R. (2010). Plant community, primary productivity, and environmental conditions following wetland re-establishment in the Sacramento–San Joaquin Delta, California. *Wetland Ecology and Management*, 18, 1–16.
- Mishra, D. R., Cho, H. J., Ghosh, S., Fox, A., Downs, C., Merani, P. B. T., et al. (2012). Post-spill state of the marsh: Remote estimation of the ecological impact of the Gulf of Mexico oil spill on Louisiana salt marshes. *Remote Sensing of Environment*, 118, 176–185.
- Moore, P. D. (1987). Ecological and hydrological aspects of peat formation. *Geological Society, London, Special Publications*, 32, 7–15.

- Morris, J. T., & Bowden, W. B. (1986). A mechanistic, numerical model of sedimentation, mineralization and decomposition for marsh sediments. *Soil Science Society of America Journal*, 50, 96–105.
- Morris, J. T., Sundareshwar, P. V., Netch, C. T., Kjerfve, B., & Cahoon, D. R. (2002). Responses of coastal wetlands to rising sea level. *Ecology*, 83, 2869–2877.
- Mutanga, O., Adam, E., & Cho, M.A. (2012). High density biomass estimation for wetland vegetation using WorldView-2 imagery and random forest regression algorithm. *International Journal of Applied Earth Observation and Geoinformation*, 18, 399–406.
- Mutanga, O., & Skidmore, A. K. (2004). Narrow band vegetation indices overcome the saturation problem in biomass estimation. *International Journal of Remote Sensing*, 25, 3999–4014.
- National Estuarine Research Reserve System (2012). Sentinel sites program guidance for understanding climate change impacts. *A guidance document for determining effects of changing sea level/lake level and inundation on coastal habitats* ((24 pp.). <http://www.nerrs.noaa.gov/Doc/PDF/Research/SentinelSiteReport2012.pdf>. Date accessed: 18 October 2013).
- Nungesser, M. K. (2011). Reading the landscape: Temporal and spatial changes in a patterned peatland. *Wetlands Ecology and Management*, 19, 475–493.
- Nyman, J., Walters, R., Delaune, R., & Patrick, J. (2006). Marsh vertical accretion via vegetative growth. *Estuarine, Coastal and Shelf Science*, 69, 370–380.
- O'Connell, J. L., Byrd, K. B., & Kelly, M. (2014). A hybrid modeling approach for mapping relative differences in belowground biomass using spectral reflectance, foliar N and plant biophysical data. (In review).
- Ollinger, S. V. (2011). Sources of variability in canopy reflectance and the convergent properties of plants. *New Phytologist*, 189, 375–394.
- Pendleton, L., Donato, D. C., Murray, B. C., Crooks, S., Jenkins, W. A., Sifleet, S., et al. (2012). Estimating global "Blue Carbon" emissions from conversion and degradation of vegetated coastal ecosystems. *PLoS ONE*, 7, e43542.
- Phinn, S. R. (1998). A framework for selecting appropriate remotely sensed data dimensions for environmental monitoring and management. *International Journal of Remote Sensing*, 19, 3457–3463.
- Phinn, S., Stow, D., & Zedler, J. (1996). Monitoring wetland habitat restoration in southern California using airborne multispectral video data. *Restoration Ecology*, 4, 412–422.
- Ramoelo, A., Skidmore, A. K., Schlerf, M., Heitkönig, I. M.A., Mathieu, R., & Cho, M.A. (2013). Savanna grass nitrogen to phosphorous ratio estimation using field spectroscopy and the potential for estimation with imaging spectroscopy. *International Journal of Applied Earth Observation and Geoinformation*, 23, 334–343.
- Rasse, D. P., Rumpel, C., & Dignac, M. -F. (2005). Is soil carbon mostly root carbon? Mechanisms for a specific stabilisation. *Plant and soil*, 269, 341–356.
- Roberts, D. A., Gardner, M., Church, R., Ustin, S., Scheer, G., & Green, R. O. (1998). Mapping chaparral in the Santa Monica Mountains using multiple endmember spectral mixture models. *Remote Sensing of Environment*, 65, 267–279.
- Rocchio, J. (2005). North American arid west freshwater marsh ecological system ecological integrity assessment. Colorado Natural Heritage Program: Fort Collins.
- Rocha, A. V., & Goulden, M. L. (2009). Why is marsh productivity so high? New insights from eddy covariance and biomass measurements in a *Typha* marsh. *Agricultural and Forest Meteorology*, 149, 159–168.
- Sadro, S., Gastil-Buhl, M., & Melack, J. (2007). Characterizing patterns of plant distribution in a southern California salt marsh using remotely sensed topographic and hyperspectral data and local tidal fluctuations. *Remote Sensing of Environment*, 110, 226–239.
- Schile, L. M., Callaway, J. C., Morris, J. T., Stralberg, D., Parker, V. T., & Kelly, M. (2014). Modeling tidal marsh distribution with sea-level rise: Evaluating the role of vegetation, sediment, and upland habitat in marsh resiliency. *PLoS ONE*, 9, e88760.
- Schmidt, K. S., & Skidmore, A. K. (2003). Spectral discrimination of vegetation types in a coastal wetland. *Remote Sensing of Environment*, 85, 92–108.
- Selvarajan, S., Mohamed, A., White, T., & Boodram, N. (2009). Assessment of geospatial technologies for natural resource management in Florida. *Journal of Forestry*, 107, 242–249.
- Serrano, L., Peñuelas, J., & Ustin, S. L. (2002). Remote sensing of nitrogen and lignin in Mediterranean vegetation from AVIRIS data: Decomposing biochemical from structural signals. *Remote Sensing of Environment*, 81, 355–364.
- Siciliano, D., Wasson, K., Potts, D. C., & Olsen, R. C. (2008). Evaluating hyperspectral imaging of wetland vegetation as a tool for detecting estuarine nutrient enrichment. *Remote Sensing of Environment*, 112, 4020–4033.
- Song, C., Woodcock, C. E., Seto, K. C., Lenney, M. P., & Macomber, S. A. (2001). Classification and change detection using Landsat TM Data: When and how to correct atmospheric effects? *Remote Sensing of Environment*, 75, 230–244.
- Stevens, M., & Hoag, C. (2000). *Plant guide – Narrowleaf cattail, Typha angustifolia L.* 4 pp. Baton Rouge, Louisiana: USDA Natural Resources Conservation Service (http://plants.usda.gov/plantguide/pdf/cs_tyan.pdf). Date accessed: 10 September 2013).
- Stralberg, D., Brennan, M., Callaway, J. C., Wood, J. K., Schile, L. M., Jongsmijt, D., et al. (2011). Evaluating tidal marsh sustainability in the face of sea-level rise: A hybrid modeling approach applied to San Francisco Bay. *PLoS ONE*, 6, e27388.
- Swanson, K. M., Drexler, J. Z., Schoellhamer, D. H., Thorne, K. M., Casazza, M. L., Overton, C. T., et al. (2013). Wetland accretion rate model of ecosystem resilience (WARMER) and its application to habitat sustainability for endangered species in the San Francisco Estuary. *Estuaries and Coasts*, 1–17.
- Thenkabail, P.S., Enclona, E. A., Ashton, M. S., Legg, C., & De Dieu, M. J. (2004). Hyperion, IKONOS, ALI, and ETM+ sensors in the study of African rainforests. *Remote Sensing of Environment*, 90, 23–43.
- Thenkabail, P.S., Enclona, E. A., Ashton, M. S., & Van Der Meer, B. (2004). Accuracy assessments of hyperspectral waveband performance for vegetation analysis applications. *Remote Sensing of Environment*, 91, 354–376.
- Thenkabail, P.S., Lyon, J. G., & Huete, A. (2012). Advances in hyperspectral remote sensing of vegetation and agricultural croplands. In P.S. Thenkabail, J. G. Lyon, & A. Huete (Eds.), *Hyperspectral remote sensing of vegetation* (pp. 28–29). Boca Raton: Taylor and Francis Group.
- Thenkabail, P.S., Mariotti, I., Gumma, M. K., Middleton, E. M., Landis, D. R., & Huemmrich, K. F. (2013). Selection of hyperspectral narrowbands (HNBs) and composition of hyperspectral two band vegetation indices (HVI) for biophysical characterization and discrimination of crop types using field reflectance and Hyperion/EO-1 Data. *IEEE Journal of Selected Topics in Applied Earth Observations and Remote Sensing*, 6, 427–439.
- Thenkabail, P.S., Smith, R. B., & De Pauw, E. (2000). Hyperspectral vegetation indices and their relationships with agricultural crop characteristics. *Remote Sensing of Environment*, 71, 158–182.
- Thenkabail, P.S., Smith, R. B., & De Pauw, E. (2002). Evaluation of narrowband and broadband vegetation indices for determining optimal hyperspectral wavebands for agricultural crop characterization. *Photogrammetric Engineering and Remote Sensing*, 68, 607–621.
- Thompson, W. R. (1935). On a criterion for the rejection of observations and the distribution of the ratio of deviation to sample standard deviation. *The Annals of Mathematical Statistics*, 6, 214–219.
- Tilley, D. (2012). *Plant guide for hardstem bulrush (Schoenoplectus acutus)*. 4 pp. Aberdeen: USDA – Natural Resources Conservation Service, Idaho Plant Materials Center (http://plants.usda.gov/plantguide/pdf/pg_scac3.pdf). Date accessed: 10 September 2013).
- Tornqvist, T. E., Wallace, D. J., Storms, J. E. A., Wallinga, J., van Dam, R. L., Blaauw, M., et al. (2008). Mississippi Delta subsidence primarily caused by compaction of Holocene strata. *Nature Geoscience*, 1, 173–176.
- Tucker, C.J. (1977). Asymptotic nature of grass canopy spectral reflectance. *Applied Optics*, 16, 1151–1156.
- Turpie, K. R. (2013). Explaining the spectral red-edge features of inundated marsh vegetation. *Journal of Coastal Research*, 29, 1111–1117.
- Tuxen, K., Schile, L., Stralberg, D., Siegel, S., Parker, T., Vasey, M., et al. (2011). Mapping changes in tidal wetland vegetation composition and pattern across a salinity gradient using high spatial resolution imagery. *Wetlands Ecology and Management*, 19, 141–157.
- USDA Forest Service (2013a). *Schoenoplectus acutus*. 1 pp. USDA Forest Service Fire Effects Information System (<http://www.fs.fed.us/database/feis/plants/graminoid/schacu/all.html>). Date accessed: 25 September 2013).
- USDA Forest Service (2013b). *Typha latifolia*. 1 pp. : USDA Forest Service Fire Effects Information System (<http://www.fs.fed.us/database/feis/plants/graminoid/typlat/all.html>). Date accessed: 25 September 2013).
- Wang, C., Menenti, M., Stoll, M. -P., Bellucco, E., & Marani, M. (2007). Mapping mixed vegetation communities in salt marshes using airborne spectral data. *Remote Sensing of Environment*, 107, 559–570.
- Whipple, A., Grossinger, R. M., Rankin, D., Stanford, B., & Askevold, R. (2012). *Sacramento-San Joaquin Delta historical ecology investigation: Exploring pattern and process*. 408 pp. Richmond: SFEI <http://www.sfei.org/DeltaHEStudy>. Date accessed: 15 September 2013.
- Zhang, M., Ustin, S. L., Rejmankova, E., & Sanderson, E. W. (1997). Monitoring Pacific Coast salt marshes using remote sensing. *Ecological Applications*, 7, 1039–1053.